THE JOURNAL OF CHEMICAL PHYSICS **128**, 124906 (2008)

Comparison of explicit atom, united atom, and coarse-grained simulations of poly(methyl methacrylate)

Chunxia Chen, Praveen Depa, and Janna K. Maranas[a]
Department of Chemical Engineering, The Pennsylvania State University, University Park, Pennsylvania 16802, USA

Victoria Garcia Sakai
NIST Center for Neutron Research, National Institute of Standards and Technology, Gaithersburg, Maryland 20899-8562, USA

(Received 12 June 2007; accepted 17 December 2007; published online 28 March 2008)

We evaluate explicit atom, united atom, and coarse-grained force fields for molecular dynamics simulation of poly(methyl methacrylate) (PMMA) by comparison to structural and dynamic neutron scattering data. The coarse-grained force field is assigned based on output of the united atom simulation, for which we use an existing force field. The atomic structure of PMMA requires the use of two types of coarse-grained beads, one representing the backbone part of the repeat unit and the other representing the side group. The explicit atom description more closely resembles dynamic experimental data than the united atom description, although the latter provides a reasonable approximation. The coarse-grained description provides structural and dynamic properties in agreement with the united atom description on which it is based, while allowing extension of the time trajectory of the simulation. © *2008 American Institute of Physics*. [DOI: 10.1063/1.2833545]

I. INTRODUCTION

Molecular dynamics (MD) simulation is extensively used for studying chemical and physical properties of a variety of materials, including polymer melts. Simulations using atomistic force fields include a high level of chemical detail, but computational resources limit the length of time trajectories. As a result, significant effort has been devoted to developing techniques that reduce computational requirements, extending both system size and trajectory length. One such technique is coarse graining (CG), which reduces computation time by removing detail: CG beads group a few atoms, monomers, or even the whole chain to a single force site. CG force fields can be generic, such as the bead-spring model[1,2] or the bond fluctuation model,[3–5] or based on an underlying atomistic description.[6–11] In the latter case, bonded and nonbonded CG potentials are derived from mapping to appropriate distribution functions from simulations with an atomistic force field. This method accurately reproduces structural properties, but since the CG force field is parameterized based only on structural information, dynamic properties evolve at an accelerated rate compared to the underlying atomistic representation.[8] For large CG force sites, static properties are matched in a similar way, and the system evolved using Langevin's equations of motion where the friction frequency can be adjusted to obtain correct dynamic properties.[12–14] Our group has parametrized CG force fields and investigated the accelerated dynamics of the resulting CG simulations for polyethylene[15] (PE) and poly(ethylene oxide) (PEO),[16] demonstrating that the origin of this "indirect speedup" is a reduced attraction to neighboring chains in the CG description. Because nonbonded interactions are less attractive, the time spent in such an interaction is reduced, and thus the system evolves at an accelerated rate. The reduced attraction occurs because the nonbonded potential which provides correct intermolecular packing has a shallower potential well than that used in underlying united atom (UA) simulations. This difference is larger in the case of PEO, resulting in a larger indirect speed up.

In this contribution, we extend our approach to polymers which require a CG side group by examining poly(methyl methacrylate) (PMMA), a well studied polymer with multiple applications due to its high transparency in visible light. Although it has been demonstrated that a CG side group is not required,[17,18] we choose to model PMMA with two types of coarse-grained beads. This allows for easier replacement of the missing atoms when going from the CG to UA representations; this is required for comparison to neutron scattering measurements, and for multiscale simulations, which combine two or more levels of modeling within the same simulation box. Our objectives are to provide a CG force field for PMMA and examine the impact of reduced chemical detail on both static and dynamic properties by comparing results of simulations using explicit atom (EA), UA, and CG force fields. We evaluate the performance of each level of modeling based on agreement with neutron scattering measurements of both structural and dynamic observables.

We present the remainder of the paper in five sections: Sec. II gives the details of the EA, UA, and CG force fields and the simulation methodology, Sec. III discusses experimental details, Sec. IV compares structural properties to neutron diffraction experiments, Sec. V compares dynamic properties to quasielastic neutron scattering experiments, and Sec. VI closes the manuscript with concluding remarks.

---

[a] Electronic mail: jmaranas@psu.edu.

© 2008 American Institute of Physics

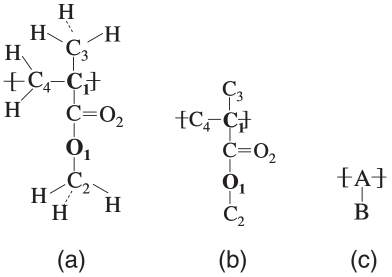

FIG. 1. The PMMA repeat unit as represented in various levels of modeling: (a) the explicit atom model, (b) the united atom model, and (c) the coarse-grained model.

II. SIMULATION DETAILS

The repeat unit of PMMA in the EA, UA, and CG representations is presented in Fig. 1. For explicit atom simulations, we use the optimized potentials for liquid simulation (OPLS) force field.[19,20] For united atom simulations, in which CH, CH_2, and CH_3 groups are treated as single force sites, we use the force field described in Ref. 21. For coarse-grained simulations, we developed a force field following the procedure used by our group[15] and others[6–8] where bonded potentials result from matching the requisite distributions obtained from UA simulations, and nonbonded potentials require coincidence of the intermolecular pair distribution function. In CG representation of PMMA, we choose to use two types of coarse grained beads, as illustrated in Fig. 1(c). The main chain atoms and the α-methyl group form coarse-grained bead A and the ester side group forms coarse-grained bead B. These coarse-grained beads are centered at C_1 and O_1 (bold in Fig. 1). This choice of grouping results in electrically neutral CG beads, and thus no electrostatic potential is used. The presence of two types of CG beads increases the number of CG potentials that must be assigned: two bond length (AA and AB) and two bending angle (AAB and AAA) potentials are required. In addition, because the CG bead A is placed at every second backbone atom, CG torsional distributions are not featureless and must also be assigned for the three types of torsional angles (AAAA, AAAB, and BAAB). The combination of these torsional potentials prevents the side group from spinning freely about the backbone. We obtain potentials from the appropriate united atom distributions by Boltzmann inversion.[22] The distributions used for nonbonded AA, AB, and AB potentials are the C_1C_1, C_1O_1, and O_1O_1 intermolecular pair distribution functions. For example, the coarse-grained, nonbonded AB potential is set based on the distribution of intermolecular C_1O_1 distances as calculated from a united atom simulation. The distributions used for bonded potentials describe the variation observed in CG bond lengths, bending angles, and torsional angles using united atom simulations. For example, the distribution function required to set the AA stretching potential is the distribution of C_1-C_1 distances as determined from UA coordinate snapshots. The CG potential parameters and the UA distributions used to set them are listed in Table I. Stretching and bending potentials are represented with analytical functions, but torsion and intermolecular potentials are stored in tabular format. When the CG force field as obtained above is

TABLE I. Bonded and nonbonded coarse-grained potential parameters.

	$u^{\mathrm{bond}}(L_{ij})=-kT\ln\{A\exp[-k_1(L_{ij}-L_{01})^2]\}$					
Bonds UA distribution	k_1 (Å^{-2})		L_{01} (Å)		A	
AA C_1C_1 distance	142.80		2.81		6.20	
AB C_1O_1 distance	111.11		2.39		5.60	
Bends UA distribution	$u^{\mathrm{bend}}(Q_{ij})=-kT\ln\{A\exp[-k_1(Q_{ij}-Q_{01})^2]+B\exp[-k_1(Q_{ij}-Q_{01})^2]\}$					
	k_1 (rad^{-2})	k_2 (rad^{-2})	Q_{01} (rad)	Q_{02} (rad)	A	B
AAA $C_1C_1C_1$ angle	32.82	82.07	2.10	2.69	0.028	0.043
AAB/BAA $C_1C_1O_1/O_1C_1C_1$ angles	35.88	10.34	1.67	1.92	0.030	0.014
	Torsions UA distribution			Nonbonded UA distribution		
	AAAA $C_1C_1C_1C_1$ dihedral			AA C_1C_1 intermolecular pair distribution function		
	AAAB $C_1C_1C_1O_1$ dihedral			AB C_1O_1 intermolecular pair distribution function		
	BAAB $O_1C_1C_1O_1$ dihedral			BB O_1O_1 intermolecular pair distribution function		
	Potentials are used in tabular form					

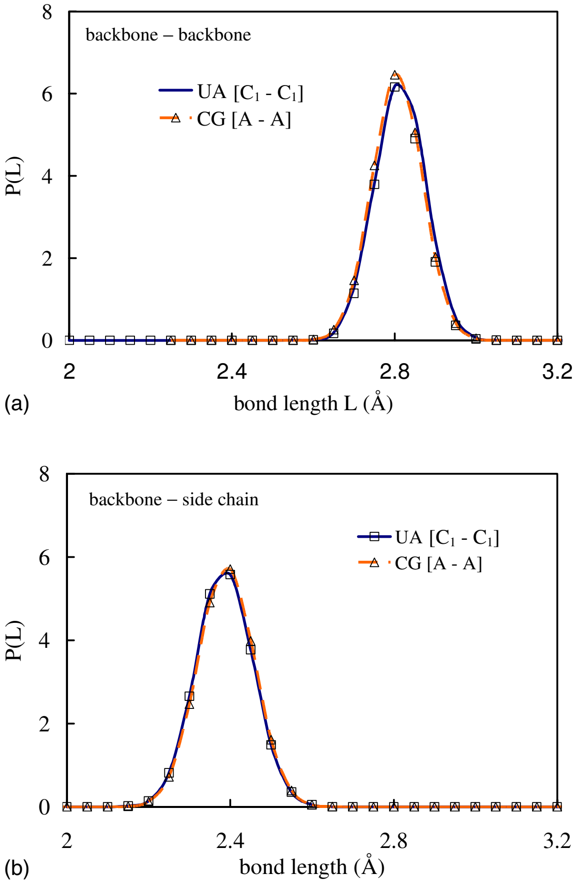

FIG. 2. (Color online) Comparison of coarse-grained bond length distributions from coarse-grained and united atom simulations: (a) backbone-backbone and (b) backbone–side chain.

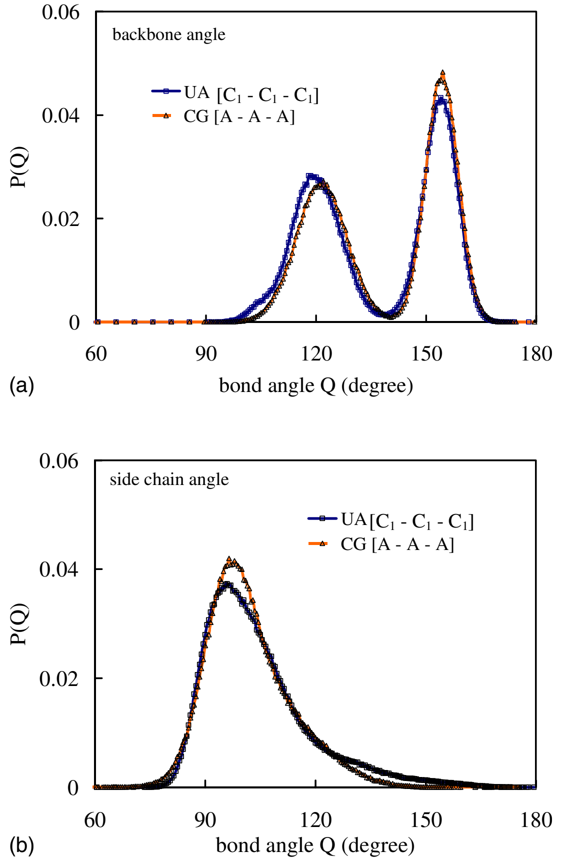

FIG. 3. (Color online) Comparison of coarse-grained bending angle distributions from coarse-grained and united atom simulations: (a) backbone angle and (b) side chain angle.

used to evolve the CG system in time, all individual distributions are maintained, as illustrated in Figs. 2–4, in which we compare the resulting CG distributions with those used for potential assignment. Coarse-grained and united atom nonbonded distributions are compared in Fig. 5, where we also examine differences from the EA level of modeling. This figure is discussed in Sec. IV.

All three simulations are performed in the *NVT* ensemble, and the temperature is maintained at 500 K using the velocity-rescaling algorithm of Berendsen *et al.*[23] The volume of the box is chosen to yield the density of atactic PMMA at 500 K ($1067\ \mathrm{kg/m^3}$).[24] Both the EA and UA force fields include electrostatic interactions: in these simulations, the Ewald summation method[25] was used to calculate the long-range Coulomb forces. Electrostatic interactions, as well as van der Waals interactions were truncated at 7 Å in EA simulations, 10 Å in UA simulations, and 15 Å in CG simulations (van der Waals interactions only). Integration was accomplished using a velocity-Verlet algorithm with a time step of 4 fs in CG simulation, and for the EA and UA simulations, the multiple time step reversible reference system propagator algorithm[26] was adopted to reduce computation time. Values for the time steps are listed in Table II.

The simulation box for all three force fields is cubic with periodic boundary conditions and contains 27 chains of atactic PMMA ($M_n = 1016\ \mathrm{g/mol}$). We note that the CG simulation does not directly preserve tacticity, in the sense that either tacticity could be obtained when reintroducing missing atoms when going from the CG to atomistic models. Tacticity is indirectly incorporated in the coarse-grained model through the CG torsional potentials, which will be different for syndiotactic and isotactic sequences. The united atom simulation box is initialized by placing identical copies of an isolated chain in a box large enough to prevent chain overlap. The isolated chain is generated by placing the backbone atoms in an all-trans configuration and then adding the ester side chains in a atactic configuration. To reduce the box size to the desired value, the molecular dynamics program is run with the box size decreasing by 10^{-4} Å every time step. Both the coarse-grained and explicit atom simulation boxes are created starting from the equilibrated UA configuration. The initial CG box is obtained by removing all but the C_1 and O_1 atoms and equating the A and B coarse-grained beads with those positions. To obtain the initial EA box from the equilibrated UA configuration, we must place two hydrogen atoms on the main chain C_4 and three on each methyl C_2 and C_3. The two hydrogen atoms are placed on the backbone carbon C_4 simultaneously, with the $C_1{-}C_4{-}H$ bond angle fixed at 110° and the $C_4{-}H$ bond length fixed at 1.09 Å. Hydrogen atoms are placed on the C_2 and C_3 methyl groups in a two-step process, described using C_2 as an example. The first hydrogen is placed with a fixed $O_1{-}C_2{-}H$ bond angle of 110°, $C_2{-}H$ bond length of 1.09 Å, and a $H{-}C_2{-}O_1{-}C$ torsional angle chosen at random. The remaining two hydrogen atoms are then inserted with $H{-}C_2{-}H$ angles of 110° and

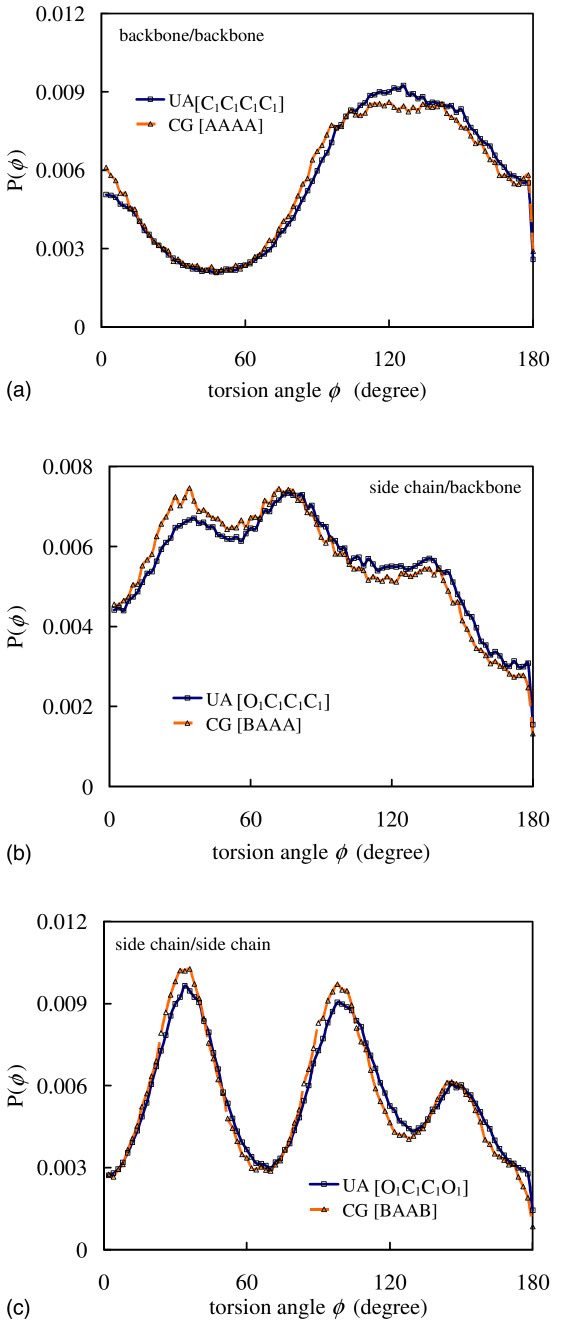

FIG. 4. (Color online) Comparison of coarse-grained torsional distributions from coarse-grained and united atom simulations: (a) backbone torsion, (b) rotation of side group around backbone, and (c) rotation of adjacent side groups.

C_2–H bond lengths of 1.09 Å. Hydrogen atoms are replaced in the same way when their positions are required to compare UA configurations to neutron measurements.

We assign the equilibration period based on the EA simulation and require that the atoms have moved at least $1R_g$ during thus time. This results in 4 ns, a time that was used for all three levels of modeling. To test for the adequacy of this assignment, we examined both structural properties $[g^{\mathrm{inter}}(r)]$ and dynamic properties $[S(q,t)]$ following the equilibration period for drift. No drifts were observed in any of the three simulations. Production runs are 4 ns for the EA and UA simulations and 8 ns for the CG simulation.

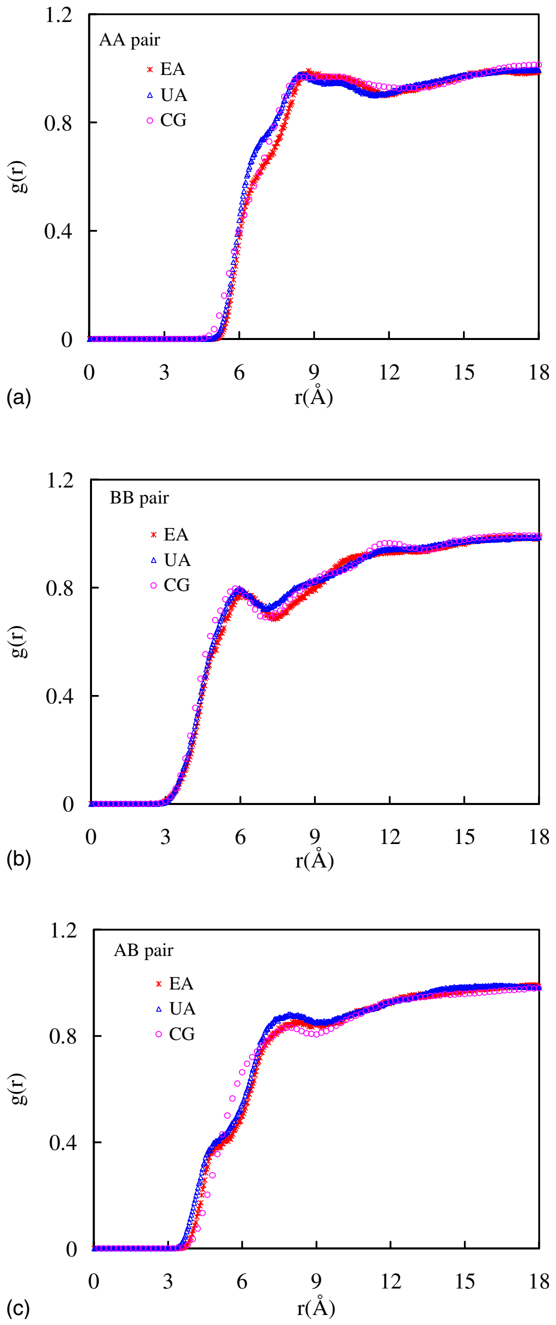

FIG. 5. (Color online) Comparison of intermolecular $g(r)$ from EA, UA, and CG simulations: (a) backbone-backbone, (b) side chain-side chain, and (c) side chain-backbone.

III. EXPERIMENTAL DETAILS

The performance of the three simulation models is assessed via comparison to neutron scattering experiments measuring structure and segmental dynamics. The structural

TABLE II. Corresponding time step for different interactions.

Interaction type	Time step (fs)
Bonding, bending, and torsion	1
Van der Waals and the real part of the Coulomb Ewald summation	2
Reciprocal part of the Coulomb Ewald Summation	4

measurements provide the static structure factor $S(q)$ and are described in Ref. 27. The segmental relaxation times are obtained from fitting decay curves covering a time range from less than 1 ps (the exact value depends on the spatial scale) to 4 ns and obtained from two neutron spectrometers. Measurements on these two instruments, the high flux backscattering spectrometer (HFBS) and the disk chopper time of flight spectrometer (DCS), both located at the National Institute of Standards and Technology Center for Neutron Research, are described below.

A. High-flux backscattering spectrometer (HFBS)

In this spectrometer, neutrons of incident wavelength 6.271 Å (E_0=2.08 meV) are Doppler shifted to achieve a range of incident energies (±20 μeV) about this nominal value.[28] The neutrons are scattered by the sample, after which only those neutrons with a final energy of 2.08 meV are detected. The dynamic range (energy transfer) of ±20 μeV sets the shortest time available to the instrument. The instrumental resolution (full width at half maximum), which sets the longest time, is dependent on the size of the Doppler shift and equal to 0.87 μeV for ±20 μeV. For data reduction purposes, this resolution was measured with a vanadium sample at 295 K. The pressed polymer sample was held in a cylindrical aluminum can mounted on a closed-cycle refrigerator unit. The thickness of the sample was around 0.1 mm, chosen to achieve 90% neutron transmission and minimize multiple scattering. The PMMA was purchased from Polymer Standards Service and has a molecular weight of 463 000 g/mol and 76% syndiotactic sequences.

B. Disk chopper time-of-flight spectrometer (DCS)

The disk chopper spectrometer uses a fixed incident wavelength, and energies of scattered neutrons are resolved by their flight times.[29] The spectrometer was operated at an incident wavelength of 4.2 Å and at a resolution of 80 μeV. The instrumental resolution was measured using a vanadium sample at 295 K with the same instrument configuration. As with HFBS, the sample was annular in shape and held in a thin-walled aluminum can mounted onto a closed-cycle refrigerator and of thickness of 0.1 mm to minimize multiple scattering. The measured quasielastic neutron scattering (QENS) spectra collected over 6 h periods were corrected for detector efficiencies using software developed at NIST [data analysis and visualization environment (DAVE)].[30] The scattering from the empty aluminum can and from the background were subtracted and the data were binned into q groups in the range of 0.60–2.60 Å^{-1}. Two hydrogenated PMMA samples were used: the one described for HFBS (463 000 g/mol and 76% syndiotactic) and one closer to the simulated molecular weight (3500 g/mol), with the same percentage of syndiotactic sequences. The glass transition temperatures measured by DSC are 397 and 373 K, respectively.

IV. STRUCTURE AND CHAIN CONFORMATION

In this section we present results on the structure and conformational properties of PMMA melts investigated by explicit atom, united atom, and coarse-grained simulations. Experiments to measure structure using neutrons reflect the positions of all the atoms in PMMA on a roughly equal basis.[27] It is thus necessary to reintroduce the missing atoms from united atom and coarse-grained simulations before comparing to this data. Because for the CG simulation, the number of missing atoms is large compared to the number of atoms that are advanced during the simulation, we compare only the EA and UA models to experimental data. The structural properties of the CG model are then assessed by comparing between all three levels of modeling.

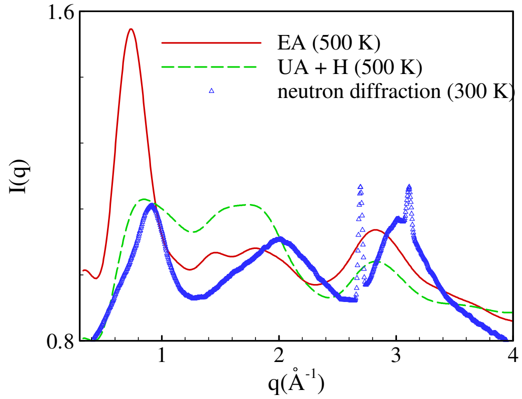

FIG. 6. (Color online) Evaluation of explicit atom and united atom descriptions for structural data. Neutron diffraction experiments (Ref. 22) are compared to scattered intensities calculated using EA and UA coordinates. UA +H: UA coordinates with hydrogen atoms reinserted and the resulting systems relaxed for 20 fs time steps.

A. Comparison to neutron diffraction

To determine the scattering intensity from simulation coordinates, we assume the sample is isotropic, in which case[31]

$$I(q)=\frac{n}{\langle|b|^2\rangle}\sum_i\sum_j c_ic_jb_ib_j\int_0^\infty[g_{ij}(r)-1]\frac{\sin qr}{qr}4\pi r^2dr, \tag{1}$$

where

$$\langle|b|^2\rangle=\sum_j c_j|b_i|^2. \tag{2}$$

Here i and j represent different atomic species, the coherent scattering length b_i describes the interaction between neutron and nucleus, the momentum transfer q defines the spatial scale, c_i is the atomic species concentration, and the total pair distribution function $g_{ij}(r)$ reflects the local packing between all atoms of types i and j.

We evaluate the UA and EA simulations against neutron diffraction data in Fig. 6. For the EA simulation, the scattered intensity, calculated from Eqs. (1) and (2), is compared directly to neutron data from Ref. 27. For the UA simulation, we first replace the missing hydrogen atoms as described in Sec. II, which places them in energetic minima. To obtain a more realistic distribution of bond lengths and angles involving hydrogen atoms, we then relax the coordinates by advancing them by 20 fs. During this time, the carbon and oxygen atom positions change by less than 0.1 Å. The UA

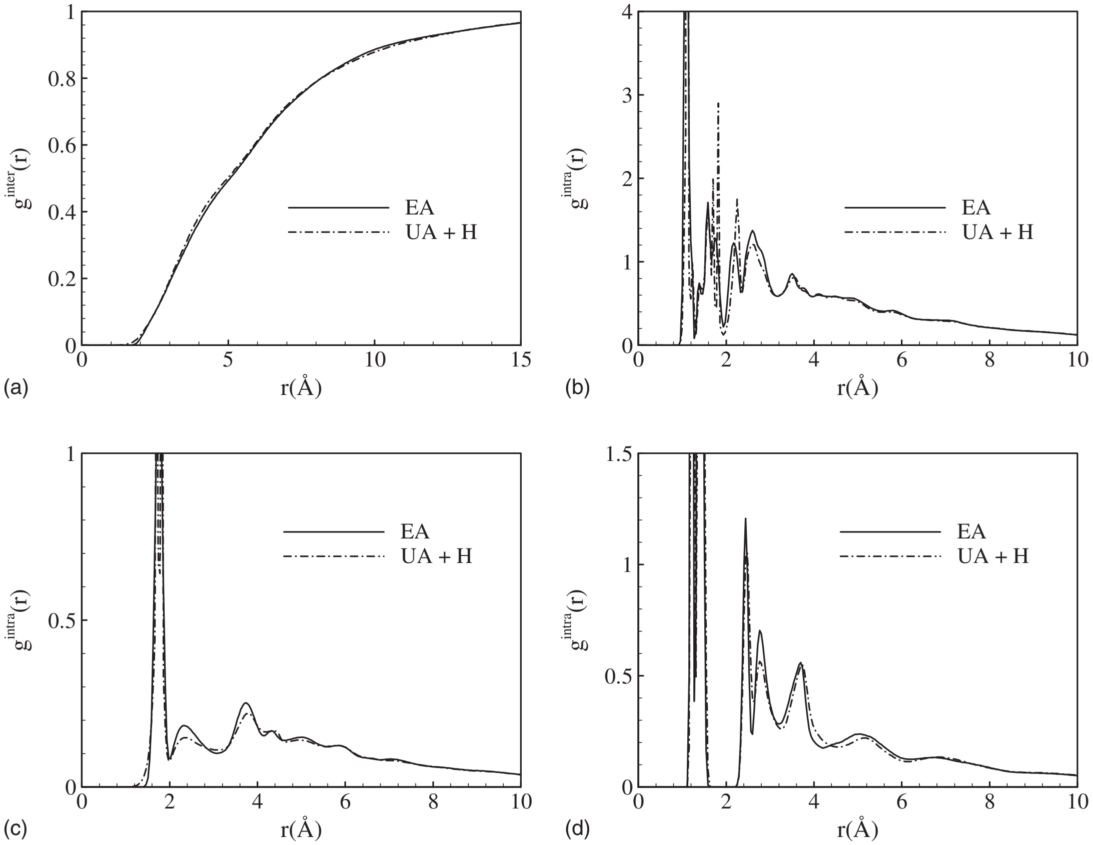

FIG. 7. Comparison of pair distribution functions from united atom and explicit atom levels of modeling: (a) intermolecular $g(r)$ using all atoms, (b) intramolecular $g(r)$ using all atoms, (c) intramolecular $g(r)$ using hydrogen atoms only, and (d) intramolecular $g(r)$ for carbon and oxygen atoms only. UA +H: UA coordinates with hydrogen atoms reinserted and the resulting systems relaxed for 20 fs.

scattered intensity shown in Fig. 6 is thus calculated following reinsertion of hydrogen atoms and relaxation of their positions. The experimental scattered intensity is not in absolute units, and the relative placement of the experimental curve on the y axis is adjusted to provide a reasonable match. The sharp peaks at $q=2.7$ Å^{-1} and $q=3.1$ Å^{-1} in the experimental data are due to the diffraction of the aluminum sample holder. None of the curves show evidence of crystallinity.

We addressed the difference between EA simulations and diffraction data in a previous publication;[32] differences in temperature between experiment and simulation cause variation in the first peak position and intensity, and differences in tacticity between simulated and experimental samples cause variation in the second and third peaks. Here we focus on differences between the UA and EA levels of description, which are evident throughout the spatial range investigated. To determine the origin of these differences, we turn to the real space analog of $S(q)$, the pair distribution function $g(r)$

$$g(r) = \frac{\langle \rho(r')\rho(r'+r)\rangle}{\langle \rho(r')\rangle^2}. \tag{3}$$

In the above, $\rho(r')$ and $\rho(r'+r)$ are the instantaneous densities of atoms at the locations r' and $r'+r$. Various specific distributions can be obtained by limiting the atoms included in the calculation. For example, we calculate the intermolecular $g(r)$ by requiring that atoms in r and r' belong to different molecules. The angular brackets indicate averages over all atom locations in the simulation box, with $\langle \rho(r')\rangle$ equal to the macroscopic density.

In Fig. 7, we compare different types of EA and UA distributions, intermolecular and intramolecular, and different types of atoms, carbon/oxygen and hydrogen. We first consider differences in intermolecular packing between the two levels of description. As supported by Fig. 7(a), the difference in the scattered intensity does not result from differences in intermolecular packing. This is unusual, because the first peak in $S(q)$ is widely regarded to be intermolecular in origin. In contrast, differences in intramolecular packing, presented in Fig. 7(b), are clearly evident. To further pinpoint their origin, we consider the intramolecular $g(r)$, calculated using hydrogen atoms [Fig. 7(c)] and carbon/oxygen atoms [Fig. 7(d)]. From comparison of these two figures, it is evident that differences exist in the intramolecular packing of all three types of atoms. Although these differences appear small, they have a large influence in reciprocal space.

D. Agreement between models

We now expand the discussion to include the CG simulations, considering agreement between all three levels of description. To evaluate the ability of the CG model in describing structural data, we consider chain dimensions and the total pair distribution function calculated using C_1 and O_1 atoms. The UA intermolecular pair distribution functions

TABLE III. Comparison of chain dimensions between explicit atom (EA), united atom (UA), and coarse-grained (CG) simulations. (No. errors are standard deviation.)

	EA	UA	CG
R_g (Å)	7.65 ± 0.66	7.77 ± 0.61	7.50 ± 0.50
R_e (Å)	18.39 ± 1.14	18.44 ± 1.18	19.30 ± 1.00

were an input to the CG model, and a comparison between the two was presented in Fig. 5. This comparison also included results from the EA model, which are in good agreement with both UA and CG data.

We assess molecular size and chain conformation by the radius of gyration (R_g) and end-to-end distance (R_e). The radius of gyration

$$R_g = \sqrt{\left\langle \frac{\Sigma_i m_i (r_i - r_{\mathrm{CM}})^2}{M} \right\rangle} \tag{4}$$

represents the average size of the chains, where M is the total chain mass and m_i is the mass of bead i. The position of bead i is indicated by r_i and the center of mass r_{CM} of each chain is $r_{\mathrm{CM}} = (\Sigma_i m_i r_i)/M$. In calculating R_g, the summation is taken over all the beads in a chain, which for the EA description are all carbon, oxygen, and hydrogen atoms, for the UA description are all carbon and oxygen atoms, and for the CG description are C_1 and O_1 atoms. The brackets indicated that an average is taken over many coordinate snapshots. The end-to-end distance

$$R_e = \langle |r_1 - r_n| \rangle \tag{5}$$

represents the average span of the chains, where r_l and r_n are the positions of the first and last carbon atoms on each chain for the UA and EA descriptions, and the first and last CG beads for the CG description. This calculation is also averaged over many coordinate snapshots. Table III illustrates that, within error, all three models provide the same chain dimensions. Thus, the different details of intramolecular packing in the EA and UA descriptions lead to differences in the structure factor, but do not influence chain dimensions.

The total pair distribution function is presented for all three levels of description in Fig. 8. This function reflects intermolecular packing, which is used to parametrize the CG force field, and intramolecular packing of C_1 and O_1 atoms. Results from the CG simulation closely follow those from the UA simulation, indicating that structural properties of the CG chains provide a reasonable description. Differences between the EA and UA descriptions discussed above remain evident.

V. DYNAMICS

Our main interest in parametrizing a coarse-grained force field for PMMA is to provide accurate dynamic information over longer times or for larger systems than is possible using atomistic simulations; for example, reptation in an entangled PMMA melt. We are also interested in the relative performance of the EA and UA descriptions for dynamic properties. To evaluate these issues, we take a similar approach as with the structural data. QENS measurements provide the correlation of hydrogen atom positions over length scales of 2–11 Å and time scales of 1 ps-5 ns. As will be shown below, this is too far removed from the applicable region of CG modeling, and thus we evaluate the performance of the simulations by comparing explicit atom and united atom data to QENS results. The performance of the CG description is then evaluated by comparison to EA and UA simulations.

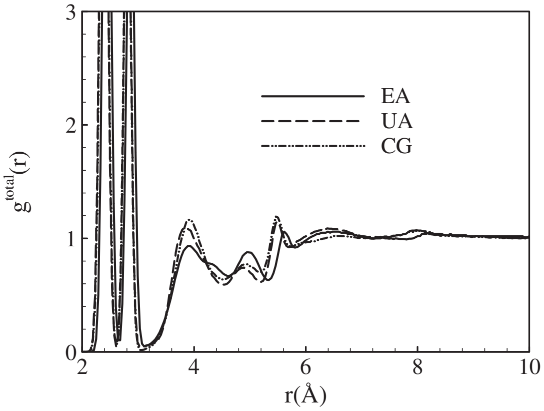

FIG. 8. Comparison of chain structure from united atom, explicit atom, and coarse-grained simulations. In each case the total pair distribution function (inter- and intramolecular pairs) using C_1 and O_1 atoms is presented at 500 K.

A. Mean squared displacement

In this section we establish the cross-over time t_c, below which the CG simulation will not provide accurate time evolution, and the indirect speed-up α, which represents the constant offset between the CG simulation and the UA simulation used to parameterize it: $\Delta t^{\mathrm{CG}} = \alpha \Delta t^{\mathrm{UA}}$. As with our previous work,[16] we do this by comparison of UA and CG squared displacements. The atomic mean squared displacement

$$\Delta r^2(t) = \langle |r_i(t + t_0) - r_i(t_0)|^2 \rangle \tag{6}$$

reflects the change in position of atom i between time t and time $t+t_0$. Brackets indicate an average over atoms and time origins t_0.

Figure 9 compares the mean squared displacements of C_1 and O_1 atoms (averaged together) from UA and CG simulations. Although it is not used to establish the indirect speed-up or crossover time, we also include the mean squared displacement from the EA simulations for comparison. We first note that the UA simulation is somewhat slower than the EA simulation; specifically, the subdiffusive plateau in the mean-squared displacement, indicative of caging, is longer in the UA description. It will be shown below that the EA description is more consistent with experimental data. The mean squared displacements for EA and UA are separated into C_1 and O_1 atoms in Fig. 9(b). Initial ballistic motion, or free motion before the cage “wall” is reached, defines a larger cage for oxygen than carbon atoms, as they are less restricted by bonding. This part of the mean-squared dis-

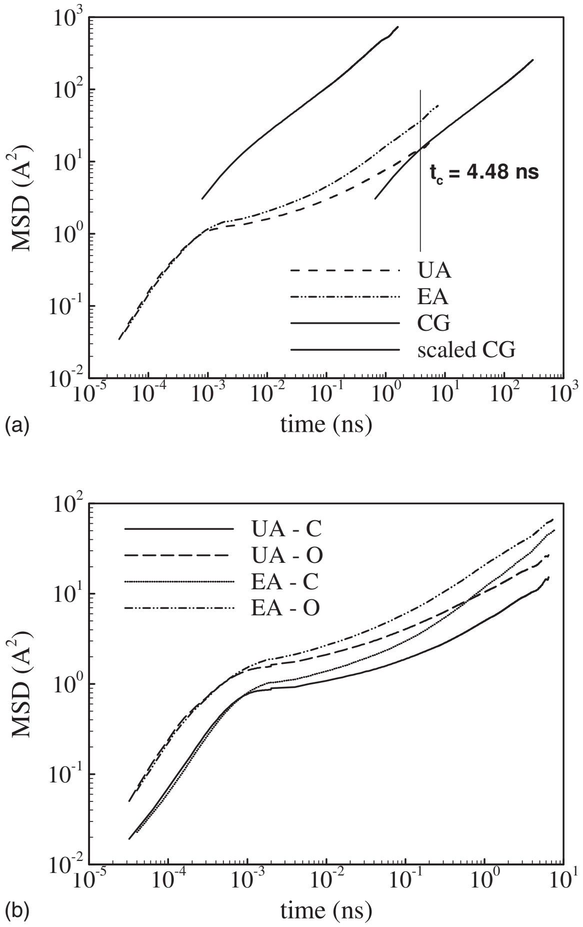

FIG. 9. Comparison of mean squared displacements from different simulation descriptions. (a) mean squared displacements of C_1 and O_1 atoms from EA, UA, and CG simulations. The scaled CG curve has been shifted along the x axis by α. (b) mean squared displacements of carbon and oxygen atoms from EA and UA simulations.

placement does not vary between EA and UA descriptions, in contrast to the plateau region, in which cage exploration in combination with subdiffusive motion of the cage center of mass occurs. Differences between the two levels of description are the same for both types of atoms. Towards the end of the available data, the mean-squared displacements of oxygen and carbon atoms approach one another, as is expected in the diffusive regime.

As with our group's work on PE (Ref. 15) and PEO,[16] the CG simulation of PMMA is faster than the UA description by a constant amount after the crossover time. The numerical value of α is controlled by differences in the CG and UA nonbonded potentials, and therefore varies with material and temperature. The value of α is determined by shifting the CG mean-squared displacement along the x axis until it coincides with the UA curve. Our prior investigations extensively verified this mapping by running the UA simulation significantly past the crossover time. In the present case, we take advantage of this verification by running the UA simulation just long enough to establish the overlap. We find that for PMMA at 500 K, $\alpha=700$. In calculating dynamic properties to follow, we obtain the correct CG time by multiplying the simulated CG time by α. The crossover time is also material dependent and appears at 15 ps for PE and 0.35 ns for PEO. For PMMA it is 4.48 ns as indicated in Fig. 9(a). The crossover time represents the time below which the CG model cannot provide an accurate description of mobility. Here we explore the reason for the variation of cross-over time between materials. We anticipate that motion below and above t_c will have different character; thus to identify this difference we consider the trajectories traced out by individual atoms within one crossover time for PEO and PMMA. This is presented as a position density plot in Fig. 10(a). The positions of 12 PEO C and 12 PMMA C_1 atoms obtained from the UA simulation are plotted over their respective crossover times: 0.35 ns for PEO and 4.48 ns for PMMA. Although the time duration for each differs, they both represent motion within one cross-over time. From the figure, it is apparent that motion over one crossover time is confined to a localized region. The size of this region is ~8 Å, which is roughly spherical with radius of ~4 Å, consistent with the average distance traveled at one crossover time apparent from the mean squared displacement, also 4 Å. To test for a change in character of mobility beyond t_c, in Fig. 10(b) we plot the positions of the same atoms, except that both PMMA and PEO are followed up to the crossover time for PMMA, 4.5 ns. In this case, the PMMA atoms are still followed over one crossover time, whereas PEO atoms are followed over ~13 cross-over times. It is evident that the character of PEO mobility is different in that each atom visits multiple local areas, such that they overlap into one continuous region. This is illustrated more clearly in Fig. 10(c), which presents trajectories of single PEO and PMMA carbon atoms over 4.5 ns. If we thus regard motion as diffusion (via hopping or continuous motion) of the center of mass of a localized site or cage, superimposed with motion within that cage, the CG model describes the series of cage locations, but not the motion within a cage. The crossover time is larger for PMMA because its local caging time is longer than that of PEO.

B. Incoherent intermediate scattering function

The QENS instruments DCS and HFBS measure the dynamic structure factor $S(q,\omega)$. In principle, the dynamic structure factor contains contributions from both coherent and incoherent scattering. However, incoherent scattering of hydrogen dominates the signal due to the large incoherent cross section of the hydrogen atom. For PMMA, incoherent scattering from hydrogen atoms contributes 97% of the experimental signal. We thus consider the incoherent dynamic structure factor of the hydrogen atoms, which is the time Fourier transform of the self-intermediate scattering function $S(q,t)$. The self-intermediate scattering function describes the correlation between the positions of hydrogen atoms at different times. We calculate it from simulation coordinates directly in reciprocal space,

$$S(q,t) = \frac{1}{N}\left\langle \sum_{i=1}^{N} \exp[-i\vec{q}\cdot(\vec{r}_i(t+t_0)-\vec{r}_i(t_0))] \right\rangle = \frac{1}{N}\left\langle \sum_{i=1}^{N} \cos(q\cdot|x_i(t+t_0)-x_i(t_0)|) \right\rangle, \quad (7)$$

where $\bar{r}_i(t)$ is the distance vector of atom i at time t, and $x_i(t)$

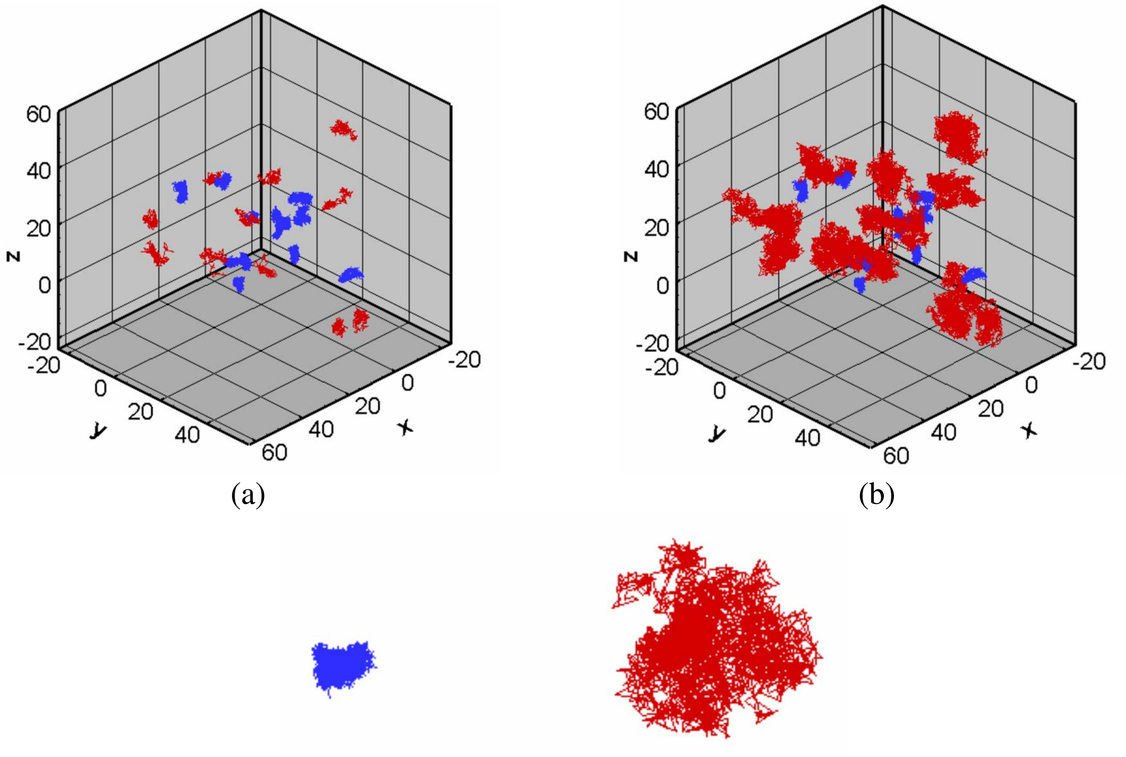

(a)

(b)

(c)

FIG. 10. (Color online) Position density graphs for PEO and PMMA: (a) time evolutions of 12 PMMA atoms and 12 PEO atoms are shown over a time interval equal to the crossover time of each: 4.5 ns for PMMA and 0.35 ns for PEO. (b) time evolutions of the same PMMA and PEO atoms as in (a), both shown over a time interval of 4.5 ns. (c) time evolutions of one PMMA and one PEO atom shown over a time interval of 4.5 ns.

the x coordinate of $\bar{r}_i(t)$. The EA simulation results are compared directly to experiment by considering hydrogen atom positions, while the three levels of modeling are compared by using C_1 and O_1 (or A and B) atom positions. Because both experiment and EA simulation capture rotation of methyl groups, a motion that is not properly represented by reinserting hydrogen atoms to the UA simulation trajectory, we do not attempt to compare the UA simulation with hydrogen atoms replaced to experimental data. The UA simulation is evaluated by comparing $S(q,t)$ as determined from carbon and oxygen positions with the same quantity from the EA simulation. Since the performance of the EA simulation is known from comparison to experiment, this allows us to evaluate the UA simulation. As described above, the CG data will not describe dynamics accurately until after the crossover time of 4.48 ns, and thus the time scales of QENS are not appropriate to test the CG model. To evaluate its performance, we consider the self-intermediate scattering function at spatial scales characteristic of chain dimensions. This is outside the spatial scale of the simulation data, and the characteristic times are larger. Although the EA and UA $S(q,t)$ at these spatial scales do not decay substantially within the trajectories collected, we evaluate the comparison of the CG by comparison of the initial portion of the decay curves and by comparison of the spatial scaling of relaxation times.

In Fig. 11 we compare two things: the experimental data with the hydrogen atom $S(q,t)$ from EA simulation and the EA simulation with UA simulation carbon and oxygen atom $S(q,t)$. The DCS and HFBS instruments cover different, but not overlapping, time windows; in the figure, the spectra are combined for comparison to simulation. For DCS, the invariance in the two different molecular weights (only one is available for HFBS) shows that the spectra are not molecular weight dependent. For both spatial scales illustrated in Fig. 11, the experimental decays agree well with the EA hydrogen atom data. As explained above, a comparison between experiment and UA data with replaced hydrogen atoms is not meaningful. Instead we include decays calculated from UA and EA coordinates using carbon and oxygen atoms, rather than hydrogen. Using the EA decays for evaluation of UA simulation results assumes that they are accurate; this is reasonable because the EA decays calculated for hydrogen agree with experimental data. As expected based on the mean squared displacements, the decays of the UA simulation are slower than those from the EA simulation, although the shapes are similar. We thus conclude that the EA simulation better represents the experimental data, but that the UA description is a reasonable substitute. We also note that the difference between the two levels of modeling appears insensitive to spatial scale.

We now consider dynamic properties from the CG description of PMMA. Plotted in Fig. 12 is the self-intermediate scattering function from the UA and CG levels of modeling, presented at two spatial scales that bracket the end-to-end distance. At these spatial scales, the decay occurs over 1000 ns, far longer than the available trajectories from UA simulation. We obtain the CG curves by adjusting the elapsed time by α, as described above. The use of CG simu-

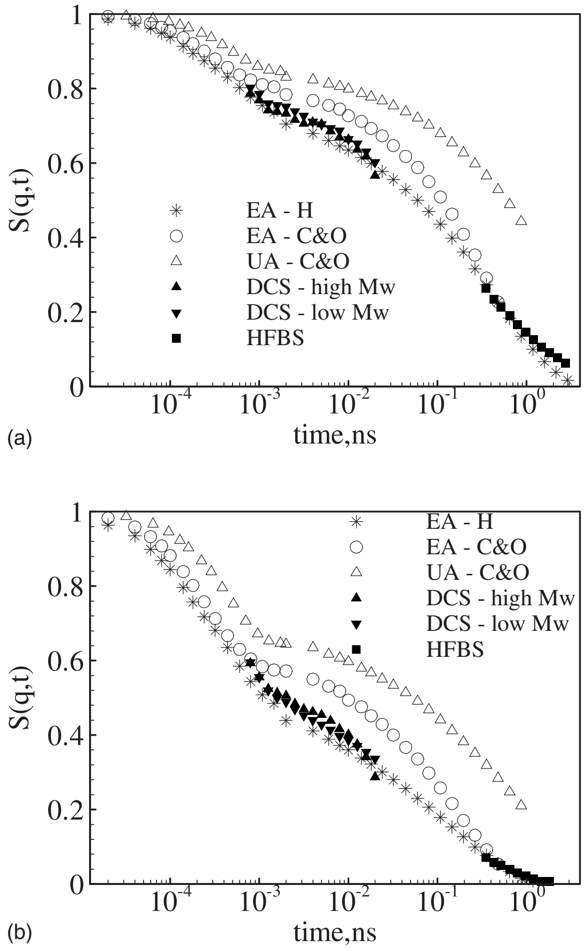

FIG. 11. Comparison of dynamic properties from experiment and simulation. The self-intermediate scattering function from experimental (solid symbols) and simulation (open symbols) data is shown with symbols explained in the figure legend: EA—H, explicit atom hydrogens; EA—C&O, explicit atom carbon and oxygen atoms; UA—C&O, united atom carbon and oxygen atoms. (a) $q=0.9$ Å^{-1} and (b) $q=1.5$ Å^{-1}.

lation thus significantly extends the range of accessible data. The CG decays merge with the UA decay at the cutoff time, whereas at earlier times the CG description is not accurate. We expect that the UA and CG data should provide a continuous decay curve, with UA data accurate at times shorter than t_c and CG data accurate at times longer than t_c. To test this, we provide a single fit, based on the CG data, but extended to times less than t_c. It is apparent from the fit line that the two levels of modeling represent the same process.

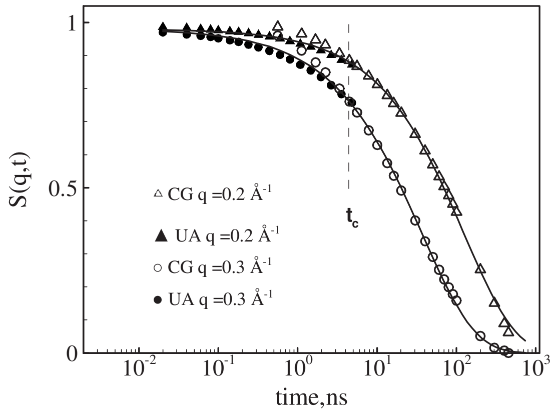

FIG. 12. Comparison of dynamic properties from united atom and coarse-grained simulation. The self-intermediate scattering function is presented at $q=0.2$ Å^{-1} (top curves) and $q=0.3$ Å^{-1} (bottom curves). In plotting the CG data, time is represented as $\alpha\Delta t$.

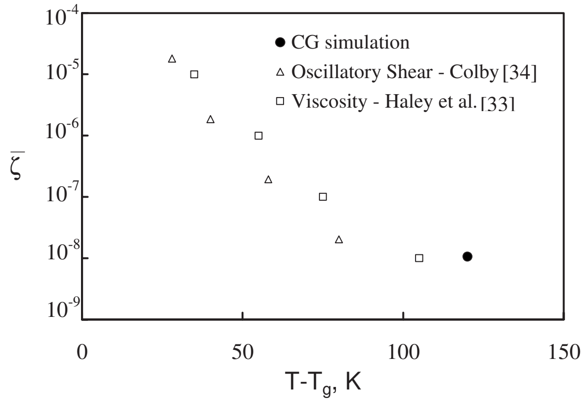

FIG. 13. Comparison of whole chain mobility between coarse-grained simulation and experiment. The monomeric friction coefficient is obtained from the center of mass mean-squared displacement (CG simulation) and viscosity measurements (Ref. 28) using the Rouse model as these systems are unentangled, and from terminal relaxation times using the reptation model for the entangled PMMA in Ref. 29.

To place the CG representation in context with experimental data, we consider motion representing whole chain, or terminal dynamics. From the CG simulations at 500 K, we have available the diffusion coefficient obtained from the center of mass mean-squared displacement (not shown) once the diffusive limit is reached. To make contact with experimental measurements, we determine the monomeric friction coefficient and compare it to two sets of data, both available over a range of temperatures: one from viscosity measurements of unentangled PMMA (Ref. 33) and the other from oscillatory shear measurements of entangled PMMA.[34] To obtain the monomeric friction coefficient corresponding to the CG diffusion coefficient, we use the Rouse model: $\zeta = kT/ND_{\rm com}$, as the PMMA in our CG simulations is not entangled. The PMMA in Ref. 33 is also unentangled; the authors used the Rouse model to relate friction coefficients to measurements of viscosity,

$$\zeta = \left(\frac{36}{N_{\rm Av}}\right)\left(\frac{1}{\rho b^2}\right)\left(\frac{M_o}{M}\right)\eta_o,$$

where η_o is the measured viscosity, $N_{\rm Av}$ is Avogadro's number, ρ is the density, b is the statistical segment length, and M and M_o are the molecular weights of the polymer and the repeat unit. To obtain the friction coefficients from the terminal relaxation times of entangled PMMA in reference,[34] we use the reptation model[35]

$$\zeta = \left(\frac{24\pi^2}{15}\right)\left(\frac{kT}{b^2}\right)\left(\frac{M_e}{M}\right)\left(\frac{M_0}{M}\right)^2\tau$$

where τ is the measured relaxation time, and M and M_e are the polymer and entanglement molecular weights. To account for differences in glass transition temperatures between the three samples, the data are presented in Fig. 13 as a function of distance above T_g. Although a stringent test is

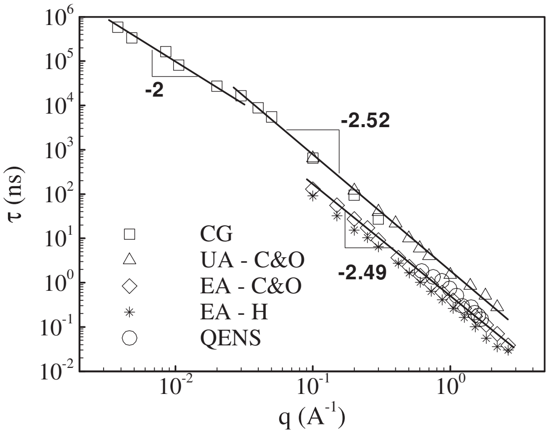

FIG. 14. Compilation of characteristic relaxation times from quasielastic neutron scattering (QENS) experiments, and explicit atom, united atom, and coarse-grained simulations. Relaxation times are determined as a function of spatial scale q at 500 K.

not possible from simulations at a single temperature, the CG data point is in reasonable agreement with the temperature dependence of both sets of experimental data.

An additional test of the performance of the CG model may be obtained by comparing the spatial dependence of characteristic times obtained from fitting the decay curves to a model function. For this purpose, we choose the Kolraush-Williams-Watts KWW function

$$S(q,t) = A \exp\left[-\left(\frac{t}{\tau_{\mathrm{KWW}}}\right)^{\beta}\right]. \tag{8}$$

In which A is a prefactor representing processes faster than the time window of fitted data, β is the width of the distribution, and τ_{KWW} is the characteristic time. At small spatial scales where pronounced two-step decay is evident, only the second part of the decay is used in this fitting process. In Fig. 14, we present the characteristic times obtained from fitting all three levels of simulation and QENS data as a function of spatial scale. As expected based on comparison of the decays themselves, the EA data more closely matches experimental results, with UA characteristic times longer by an amount that is q independent. Within the range where both UA and CG data are complete enough to provide satisfactory fits and extract characteristic times, the two are in excellent agreement. At larger spatial scales, the CG data changes slope, indicating a change in the character of the motion probed. Based on the spatial scale where this occurs (several R_e) and the new slope (-2), this represents diffusive motion of the entire chain.

VI. CONCLUDING REMARKS

We have compared explicit atom, united atom, and coarse-grained descriptions of PMMA, with the goal of providing a comprehensive view of mobility using simulation. A large range of motions occur in PMMA: secondary relaxations such as the β-relaxation and methyl group rotations, the structural relaxation, and whole chain motion that depends on molecular weight and entanglement. To properly study the entire range, a combination of different descriptions is required. The explicit atom description is necessary to observe methyl group rotation, the united atom representation allows longer trajectories for segmental processes that are adequately captured by motion of atoms other than hydrogen, and a coarse-grained approach is required to study entanglement or reptation. Here we show that all three representations are in adequate agreement with experimental data, and thus provide a suite of tools with which PMMA mobility may be examined using simulation. Although we use short chains that are unentangled for the current study, so that all three levels of modeling may be compared, the utility of a coarse-grained model lies in the ability to simulate longer chains either directly or as an equilibration tool for subsequent all atom simulations.[36]

ACKNOWLEDGMENTS

We gratefully acknowledge financial support from the National Science Foundation, Polymers Program under Grant No. DMR-0134910 and the Department of Energy, Mathematical and Information Sciences under Grant No. DE-FG02-02ER25535. This work utilized facilities supported in part by the National Science Foundation under Agreement No. DMR-0454672.

[1] P. O. Brunn, J. Chem. Phys. **80**, 5821 (1984).
[2] R. B. Bird, O. Hassager, R. C. Armstrong, and C. F. Curtiss, *Kinetic Theory*, Dynamics of Polymeric Liquids, Vol. II (Wiley, New York, 1977).
[3] N. B. Wilding, M. Müller, and K. Binder, J. Chem. Phys. **105**, 802 (1996).
[4] W. Paul, K. Binder, D. W. Heerman, and K. Kremer, J. Chem. Phys. **95**, 7726 (1991).
[5] I. Carmesin and K. Kremer, Macromolecules **21**, 2819 (1988).
[6] L. Whitehead, C. M. Edge, and J. W. Essex, J. Comput. Chem. **22**, 1622 (2001).
[7] C. F. Lopez, S. O. Nielsen, P. B. Moore, J. C. Shelley, and M. L. Klein, J. Phys.: Condens. Matter **14**, 9431 (2002).
[8] C. F. Lopez, P. B. Moore, J. C. Shelley, M. Y. Shelley, and M. L. Klein, Comput. Phys. Commun. **147**, 1 (2002).
[9] W. Tschöp, K. Kremer, J. Batoulis, T. Bürger, and O. Hahn, Acta Polym. **49**, 61 (1998).
[10] K. Kremer and F. Müller-Plathe, MRS Bull. **26**, 205 (2001).
[11] J. Baschnagel, K. Binder, P. Doruker *et al.*, Adv. Polym. Sci. **152**, 41 (2000).
[12] R. L. C. Akkermans and W. J. Briels, J. Chem. Phys. **113**, 6409 (2000).
[13] J. T. Padding and W. J. Briels, J. Chem. Phys. **117**, 925 (2002).
[14] J. T. Padding and W. J. Briels, J. Chem. Phys. **115**, 2846 (2001).
[15] P. K. Depa and J. K. Maranas, J. Chem. Phys. **123**, 094901 (2005).
[16] C. X. Chen, P. Depa, V. García Sakai, J. K. Maranas, J. W. Lynn, I. Peral, and J. R. D. Copley, J. Chem. Phys. **124**, 234901 (2006).
[17] V. A. Harmandaris, N. P. Adhikari, N. F. A. vanderVegt, and K. Kremer, Macromolecules **39**, 6708 (2006).
[18] G. Milano and F. Muller-Plathe, J. Phys. Chem. B **109**, 18609 (2005).
[19] K. Kahn and T. C. Bruice, J. Comput. Chem. **23**, 977 (2002).
[20] M. L. P. Price, D. Ostrovsky, and W. L. Jorgensen, J. Comput. Chem. **22**, 1340 (2001).
[21] O. Okada, K. Oka, S. Kuwajima, S. Toyoda, and K. Tanabe, Comput. Theor. Polym. Sci. **10**, 371 (2000).
[22] D. Reith, M. Pütz, and F. Müller-Plathe, J. Comput. Chem. **24**, 1624 (2003).
[23] H. J. C. Berendsen, J. P. M. Postma, W. F. Van Gunsteren, A. Di Nola, and J. R. Heak, J. Chem. Phys. **81**, 3684 (1984).
[24] W. Wunderlich, in *Polymer Handbook*, 3rd ed., edited by J. Brandrup and E. H. Immergut (Wiley, New York, 1989), Sec. V, p. 77.
[25] P. Ewald, Ann. Phys. **64**, 253 (1921).
[26] M. Tuckerman, B. J. Berne, and G. J. Martyna, J. Chem. Phys. **97**, 1990 (1992).
[27] B. Farago, C. X. Chen, J. K. Maranas, S. Kamath, R. H. Colby, A. J. Pasquale, and T. E. Long, Phys. Rev. E **72**, 031809 (2005).

[28] A. Meyer, R. D. Dimeo, P. M. Gehring, and D. A. Neumann, Rev. Sci. Instrum. **74**, 2762 (2003).
[29] R. D. Copley and J. C. Cook, Chem. Phys. **292**, 477 (2003).
[30] The IDL-based program can be found at http://www.ncnr.nist.gov/dave
[31] O. Borodin, R. J. Douglas, G. D. Smith, F. Trouw, and S. Petrucci, J. Phys. Chem. B **107**, 6813 (2003).
[32] C. X. Chen, J. K. Maranas, and V. García Sakai, Macromolecules **39**, 9630 (2006).
[33] J. C. Haley and T. P. Lodge, J. Chem. Phys. **122**, 234914 (2005).
[34] R. H. Colby, Polymer **30**, 1275 (1989).
[35] J. C. Haley, T. P. Lodge, Y. He, M. D. Ediger, E. D. von Meerwall, and J. Mijovic, Macromolecules **36**, 6142 (2003).
[36] B. Hess, S. León, N. van der Vegt, and K. Kremer, Soft Matter **2**, 409 (2006).